JOURNAL OF THE AMERICAN CHEMICAL SOCIETY
pubs.acs.org/JACS
Article

Strong d−π Orbital Coupling of Co−C$_4$ Atomic Sites on Graphdiyne Boosts Potassium−Sulfur Battery Electrocatalysis

Shipeng Zhang, Ya Kong, Yu Gu, Ruilin Bai, Menggang Li, Shuoqing Zhao, Mingze Ma, Zhen Li, Lingyou Zeng, Daping Qiu, Qinghua Zhang, Mingchuan Luo, Lin Gu, Yan Yu,* Shaojun Guo,* and Jin Zhang*

Cite This: *J. Am. Chem. Soc.* 2024, 146, 4433−4443

Read Online

ACCESS | Metrics & More | Article Recommendations | SI Supporting Information

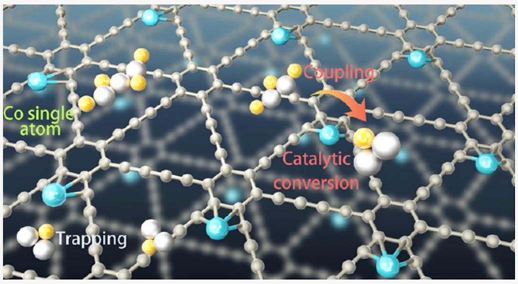

ABSTRACT: Potassium−sulfur (K−S) batteries are severely limited by the sluggish kinetics of the solid-phase conversion of K_2S_3/K_2S_2 to K_2S, the rate-determining and performance-governing step, which urgently requires a cathode with facilitated sulfur accommodation and improved catalytic efficiency. To this end, we leverage the orbital-coupling approach and herein report a strong d−π coupling catalytic configuration of single-atom Co anchored between two alkynyls of graphdiyne (Co-GDY). The d−π orbital coupling of the Co−C$_4$ moiety fully redistributes electrons two-dimensionally across the GDY, and as a result, drastically accelerates the solid-phase K_2S_3/K_2S_2 to K_2S conversion and enhances the adsorption of sulfur species. Applied as the cathode, the S/Co-GDY delivered a record-high rate performance of 496.0 mAh g^{-1} at 5 A g^{-1} in K−S batteries. *In situ* and *ex situ* characterizations coupling density functional theory (DFT) calculations rationalize how the strong d−π orbital coupling of Co−C$_4$ configuration promotes the reversible solid-state transformation kinetics of potassium polysulfide for high-performance K−S batteries.

■ INTRODUCTION

Potassium−sulfur (K−S) batteries are receiving great attention for large-scale energy storage due to their high energy density (1023 Wh kg^{-1}), high element abundance (both potassium and sulfur), environmental benignity, and low cost.[1−6] However, further advancement of K−S batteries has encountered challenges associated with volume expansion and electronic insulation nature of sulfur, the shuttle effect of potassium polysulfide, and sluggish kinetics.[7−9] Compared to the inseparable low-order polysulfides in Li/Na−S batteries, K−S batteries have explicit cathode electrochemistry, which involves both solution-phase and solid-phase processes.[10−20] Among them, the solid-phase K_2S_3/K_2S_2 to K_2S process delivers over 60% of the theoretical capacity; however, in reality, the excessively high reaction barrier and the discharge production of "dead" sulfur species (partial K_2S) induce significant capacity loss for the K−S batteries.[21] Therefore, the sluggish kinetics of the K_2S_3/K_2S_2 to K_2S conversion has become one of the grand challenges affecting the capacity, rate ability, and capacity retention of K−S batteries.[22,23] To solve this problem, intermetallics, metal nanoparticles, single-atom catalysts, and homogeneous catalysts have been explored as potassium polysulfide catalysts, aiming to facilitate the conversion of sulfur.[24−26] Despite these endeavors, the solid-state conversions of K_2S_3/K_2S_2 to K_2S are still sluggish, and the respective mechanism remains elusive, which collectively restrict further advancement of K−S batteries. Therefore, the search for new-concept cathodes with much improved catalytic activities toward the solid-state conversions of K_2S_3/K_2S_2 to K_2S is highly desirable, *yet* remains a grand challenge.

Herein, we report a class of Co−C$_4$ atomic sites anchored on ultrathin graphdiyne (GDY) nanosheets (Co-GDY) as a highly efficient cathode for K−S batteries. Our motivation of using GDY lies in its unique features of sp- and sp^2-hybridized carbon atoms, highly π-conjugated structure, and special pore structure of hexagon benzene rings connected by diacetylenic linkings,[27−32] potentially conducive to the adsorption and conversion of sulfur.[33−38] We first demonstrate a strong π−d coordination between two alkynyl groups of GDY and Co single atoms, originating from the highly electronegative −C≡C−C≡C− group. As a result, the as-prepared S/Co-GDY cathode simultaneously delivers a high current density of 5 A g^{-1}, an excellent rate performance of 496 mAh g^{-1}, a high capacity of 1064 mAh g^{-1} after 180 cycles at 0.2 A g^{-1}, and a long lifespan over 500 cycles at 1 A g^{-1} with the low average capacity degradation of only 0.08% per cycle. The S/Co-GDY cathode also significantly advances Na−S batteries by showing

Received: September 6, 2023
Revised: January 16, 2024
Accepted: January 17, 2024
Published: February 8, 2024

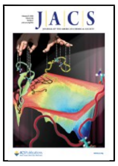

https://doi.org/10.1021/jacs.3c09533

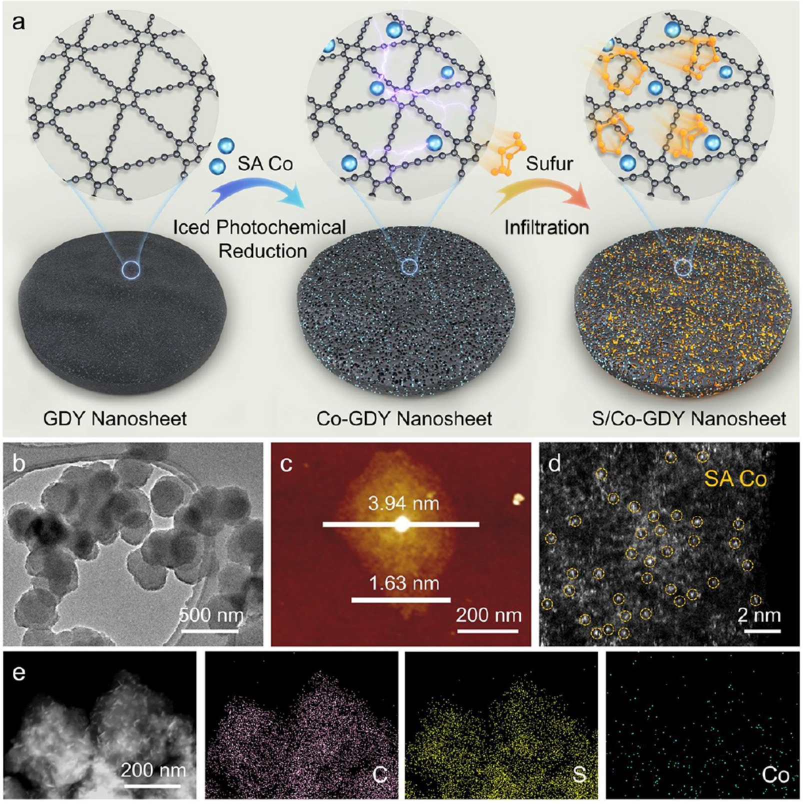

Figure 1. (a) Illustration of the synthesis of the S/Co-GDY nanosheet. (b, c) TEM and AFM images of the ultrathin circular GDY nanosheet. (d) Atomic-resolution HAADF-STEM image of S/Co-GDY. (e) Corresponding elemental mapping images of the S/Co-GDY nanosheet.

the best rate performance (725 mAh g^{-1} at 5 A g^{-1}) at room temperature. Various *in situ* and *ex situ* experimental techniques, precipitation experiments, and density functional theory (DFT) calculations collectively revealed that d−π orbital coupling of Co−C_4 atomic sites facilitated the charge transfer efficiency of sulfur to potassium polysulfide, verifying the super catalytic ability of Co-GDY as sulfur host for K−S batteries.

■ RESULTS AND DISCUSSION

Figure 1a illustrates the preparation process for making the single-atom Co embedded in ultrathin GDY nanosheets a superior host for sulfur (S/Co-GDY). The GDY nanosheets were first synthesized by a microwave-assisted catalysis technology via the dissolution of hexynylbenzene in homogeneous organic solutions using copper salts as the catalyst. Then, the single-atom Co was anchored on the surface of GDY nanosheets through π-coordination based on the electronegativity difference between the high-reactive sp-hybridized carbon atoms of the GDY and single-atom Co. After that, the sulfur was infiltrated into the GDY nanosheets with particularly high porosity and specific surface area to yield the S/Co-GDY cathode.

Transmission electron microscopy (TEM), atomic force microscopy (AFM), and high-angle annular dark-field scanning transmission electron microscopy (HAADF-STEM) were used to characterize the structure of the prepared materials. Figure 1b,c display the ultrathin circular GDY nanosheets with a diameter of around 200 nm and a thickness of only about 4 nm. TEM images of the Co-GDY and S/Co-GDY nanosheets (Figure S1a,b) reveal that there is almost no change in morphology after immobilizing single-atom Co and sulfur. The aberration-corrected HAADF-STEM of Co-GDY and S/Co-GDY (Figure 1d and S2) show that it has massive bright spots on its surface, attributed to single-atom Co. The corresponding energy dispersive spectroscopy (EDS) mapping of S/Co-GDY confirms the uniform distribution of C, S, and Co elements over GDY nanosheets (Figures 1e and S3).

The X-ray diffraction (XRD) patterns of GDY, Co-GDY, and S/Co-GDY nanosheets (Figure S4) validate the absence of characteristic peaks related to Co species, indicating that Co nanoparticles do not exist on the Co-GDY and S/Co-GDY. In addition, the weaker characteristic peaks of sulfur for S/Co-GDY prove that most of the sulfur is uniformly infiltrated into the porous structure of the GDY nanosheets. The S loading amount of the S/Co-GDY and S/GDY was determined to be 50.2 and 53.6 wt %, respectively, by thermogravimetric analysis (TGA, Figure S5). The prepared GDY host was verified by Raman spectroscopy (Figure 2a), revealing that three diffraction peaks at 1417, 1558, and 2173 cm^{-1} correspond to the D band, G band, and conjugated diyne linkage, respectively. The intensity of the diffraction peak at 2173 cm^{-1} represents the content of −C≡C−C≡C−, further demonstrating the high efficiency of the coupling reaction.[39,40] Raman spectroscopy of the Co-GDY shows the weaker broad peak of the −C≡C−C≡C− (Figure S6), indicating that partial conjugated carbon atoms were broken with single-atom Co to form Co−C atomic sites, which demonstrates the strong orbital coupling between the d-orbital of the single-atom Co and the π-orbital of the conjugated carbon atoms. The high-resolution X-ray photoelectron spectroscopy (XPS) spectra of Co-GDY and S/Co-GDY are shown in Figures S7 and S8. Figure S7a displays the XPS spectrum of C 1s for the Co-GDY

https://doi.org/10.1021/jacs.3c09533
J. Am. Chem. Soc. 2024, 146, 4433−4443

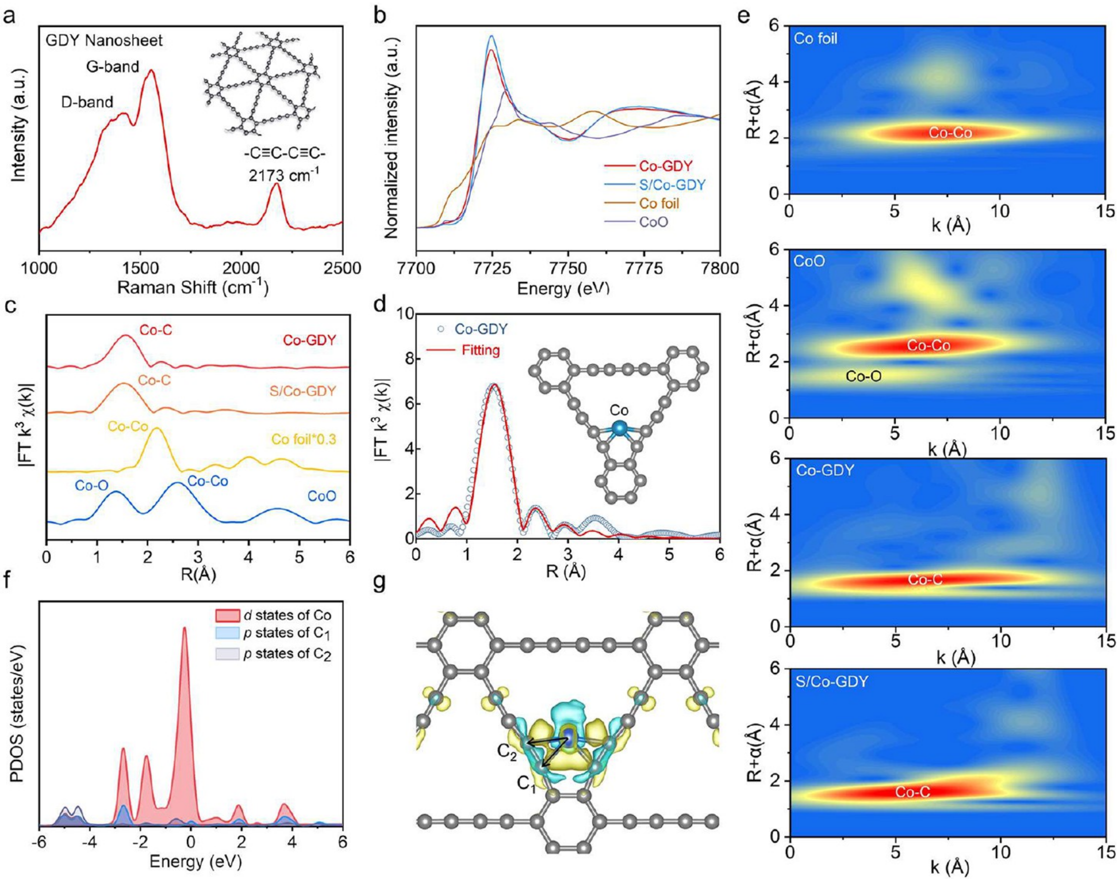

Figure 2. (a) Raman spectra of pristine GDY nanosheet. (b, c) XANES spectra at the Co K-edge and Fourier-transform EXAFS spectra of Co-GDY, S/Co-GDY, Co foil, and CoO. (d) EXAFS fitting curves of Co-GDY in R space. Inset: corresponding atomic structures. (e) Wavelet transform plots for the EXAFS signal of the Co-GDY, S/Co-GDY, Co foil, and CoO, respectively. (f) Projected density of states of the interface Co−C atoms in Co-GDY. (g) The charge density difference of the Co−C_4 atomic site anchored on GDY.

nanosheets. The four peaks at 284.4, 285.2, 286.2, and 287.7 eV were identified as C−C (sp^2), C−C (sp), C−O, and C═O, respectively. The two strongest peaks of C−C (sp) and C−C (sp^2) prove the component of carbon atoms in GDY derives from sp- and sp^2-hybridized carbon atoms. Four peaks identified at 779.6, 786.3, 794.1, and 798.3 eV correspond to the Co $2p_{3/2}$, Sat., Co $2p_{1/2}$, and Sat., respectively (Figure S7b), indicating that the Co-GDY contains small amounts of Co.[41]

To further analyze the atomic structure and coordination environment of Co element in Co-GDY and S/Co-GDY samples, the X-ray absorption near edge structure (XANES) and extended X-ray absorption fine structure (EXAFS) of S/Co-GDY and two standard references (Co foil and CoO) were observed (Figures 2b and S9−S11). The adsorption edge positions of Co-GDY and S/Co-GDY were located between those of the Co foil and CoO, indicating that the valence state of single-atom Co in Co-GDY and S/Co-GDY was found to be between the Co^0 and Co^{II}. Figure 2c shows the Fourier transform (FT) k^2-weighted EXAFS spectra of Co-GDY and S/Co-GDY and standard references. The spectrum of Co-GDY and S/Co-GDY demonstrated the strong peak at about 1.55 Å, illustrating the formation of Co−C bonds. The relevant fitted parameters are shown in Figure 2d and Table S1, and the coordination number (CN) and the bond length of the Co−C bond from Co−C_4 atomic sites are both about 4.12 and 2.02, demonstrating that single-atom Co was coordinated by four carbons from the diyne linkage at the active center of GDY. The inset in Figure 2d is the structure model of the atomically dispersed S/Co-GDY site. To further establish the atomic dispersion of single-atom Co in S/Co-GDY, the wavelet transform (WT) analysis was carried out (Figure 2e), identifying the backscattering atoms and providing the enhanced resolution in R and K space. The WT contour plot of Co-GDY and S/Co-GDY only display a significant intensity maximum, correlating with Co−C scattering, which differs from the Co−Co bond in the Co foil and the Co−O bond in CoO.[42] The mass content of single-atom Co in the Co-GDY sample was determined to be 0.61 wt % by inductively coupled plasma mass spectrometry (ICP-MS).

The p_x−p_y π/π^*-orbitals of −C≡C−C≡C− can freely rotate around the Co−C bonds, and the Co atom is coordinated by the overlapping π/π^*-orbitals of two alkynyl groups, forming a Co−C_4 structure.[43] By analyzing the projected density of states (PDOS) of single-atom Co and sp-hybridized carbon atoms (Figures 2f and S12), the high overlapping between the d-orbital of single-atom Co and the p-orbitals of sp-hybridized carbon atoms (C_1 and C_2) was verified, demonstrating the strong d−π orbital coupling of Co−C_4 atomic sites. The space charge distribution around two alkynyl groups and single-atom Co was analyzed by the Co-GDY charge difference density (Figure 2g). Due to the strong electron-withdrawing effect of −C≡C−C≡C− structure and the orbital hybridization of the Co−C_4 structure, the charge of

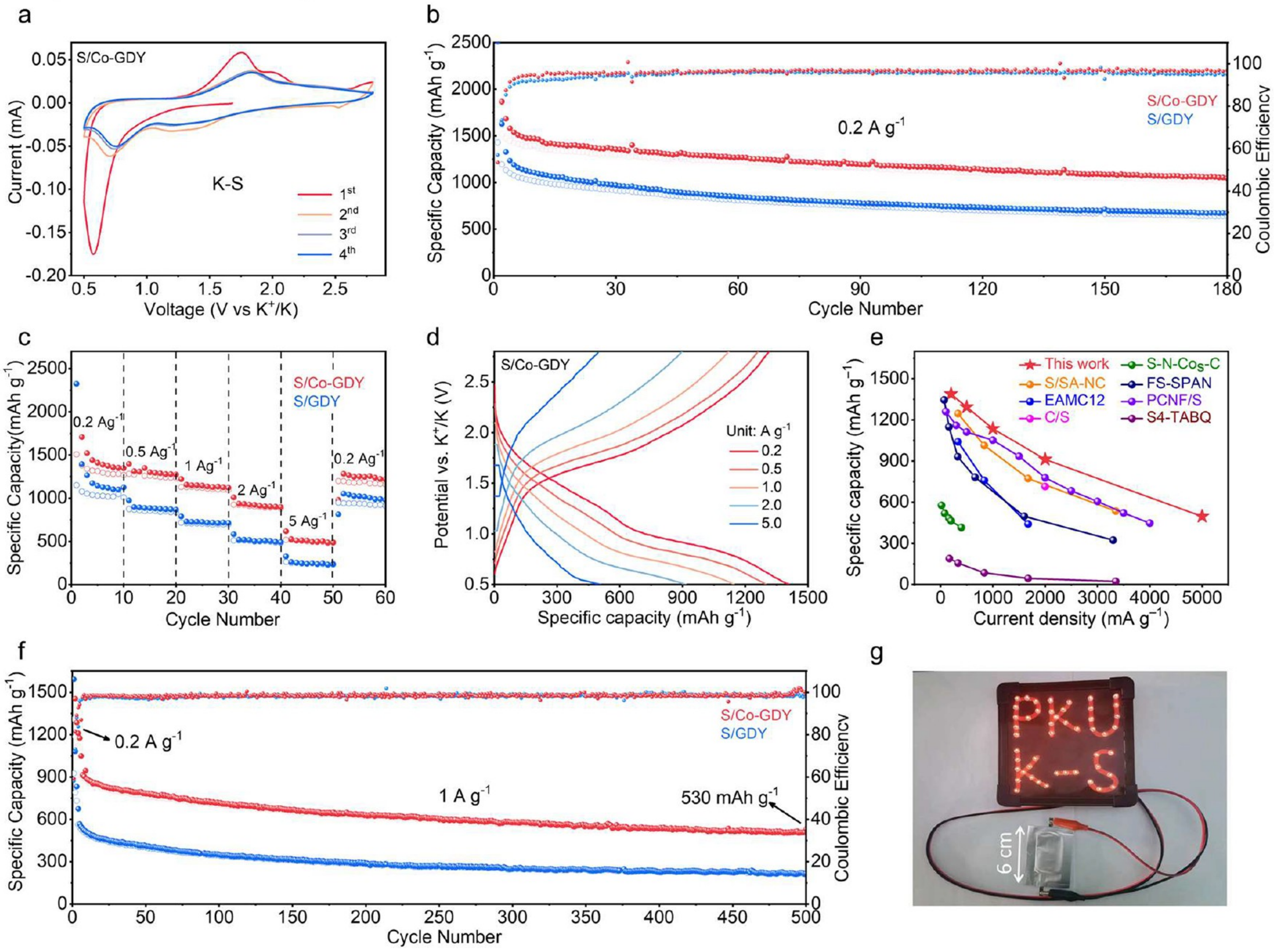

Figure 3. Electrochemical properties of the S/Co-GDY and S/GDY cathodes for K−S batteries: (a) Initial four CV curves of the S/Co-GDY cathodes at 0.1 mV s^{-1}. (b) Cycling performances of the S/Co-GDY and S/GDY cathodes at 0.2 A g^{-1}. (c) Rate capabilities at the current densities from 0.2 to 5 A g^{-1} of S/Co-GDY and S/GDY samples and (d) corresponding charge−discharge profiles of the S/Co-GDY. (e) A comparison of the S/Co-GDY cathode with recently reported cathodes for K−S batteries. (f) Long-term cycling stability of S/Co-GDY and S/GDY cathodes at 1 A g^{-1} for 500 cycles. (g) The optical image of the lighted LED using a K−S pouch cell with a S/Co-GDY cathode.

the d-orbital for the Co atom is transferred to the π-orbital of the alkynyl carbon to form the π-coordination structure, and the charge deletion of the d-orbital for single-atom Co can coordinate with the p-orbital of sulfur.

The unique Co−C$_4$ with strong d−π orbital coupling coordinated by alkyne bonds enables us to investigate the conversion efficiency of sulfur for K−S batteries in the voltage window of 0.5−2.8 V (vs K$^+$/K). Figures 3a and S13 show the cyclic voltammograms (CVs) of the S/Co-GDY and S/GDY at 0.1 mV s^{-1} for the first four cycles. In the initial cycle, the reduction peak at about 0.5 V corresponds to the conversion from K$_2$S$_3$/K$_2$S$_2$ to K$_2$S, which is the key step from sulfur to potassium polysulfide. The stronger reduction peak of the S/Co-GDY than that of the S/GDY indicates that the strong d−π orbital coupling of the Co−C$_4$ atomic sites on the GYD facilitates the conversion kinetics from K$_2$S$_3$/K$_2$S$_2$ to K$_2$S. In the follow-up cycles, the overlapping CVs demonstrate the superior redox stability of S/Co-GDY. The galvanostatic charge−discharge profiles of S/Co-GDY show the typical voltage plateaus to match the CV results (Figure S14). The low initial Coulombic efficiencies of S/Co-GDY and S/GDY cathodes can be attributed to the formation of a solid-electrolyte interphase (SEI). The XPS analysis after the S/Co-GDY cathode is discharged to 0.8 V was used to investigate the SEI. As shown in Figure S15, the F 1s spectra showed the presence of a K−F bond (683 eV) and a C−F bond (689 eV).

Figure 3b shows the cycling performance of the S/Co-GDY and S/GDY cathodes at a current density of 0.2 A g^{-1}. Obviously, the S/Co-GDY cathode exhibits a high discharge capacity of 1046 mAh g^{-1} with a high Coulombic efficiency (CE) of ∼100% after 180 cycles. In contrast, the S/GDY cathode only demonstrates a lower discharge capacity of 673.0 mAh g^{-1} after 180 cycles. The S/Co-GDY cathode can deliver high discharge capacities of 1388.0, 1294.0, 1136.0, 912.0, and 496.0 mAh g^{-1} under current densities of 0.2, 0.5, 1, 2, and 5 A g^{-1}, respectively, much higher than those of the S/Co-GDY cathode (1128, 881, 717, 506, and 246 mAh g^{-1} at 0.2, 0.5, 1, 2, and 5 A g^{-1}) (Figure 3c). In addition, the thick electrode of S/Co-GDY (1.2 mg cm^{-2}) (Figure S16) delivers high reversible capacities of 709.0 mAh g^{-1} at 0.2 A g^{-1} after 50 cycles and 512 mAh g^{-1} at 0.5 A g^{-1} after 60 cycles, respectively. And, the S/Co-GDY electrode with high sulfur ratio (71.7 wt %) (Figure S17) could deliver a high capacity of 609.0 mAh g^{-1} at 0.2 A g^{-1} after 50 cycles. The galvanostatic

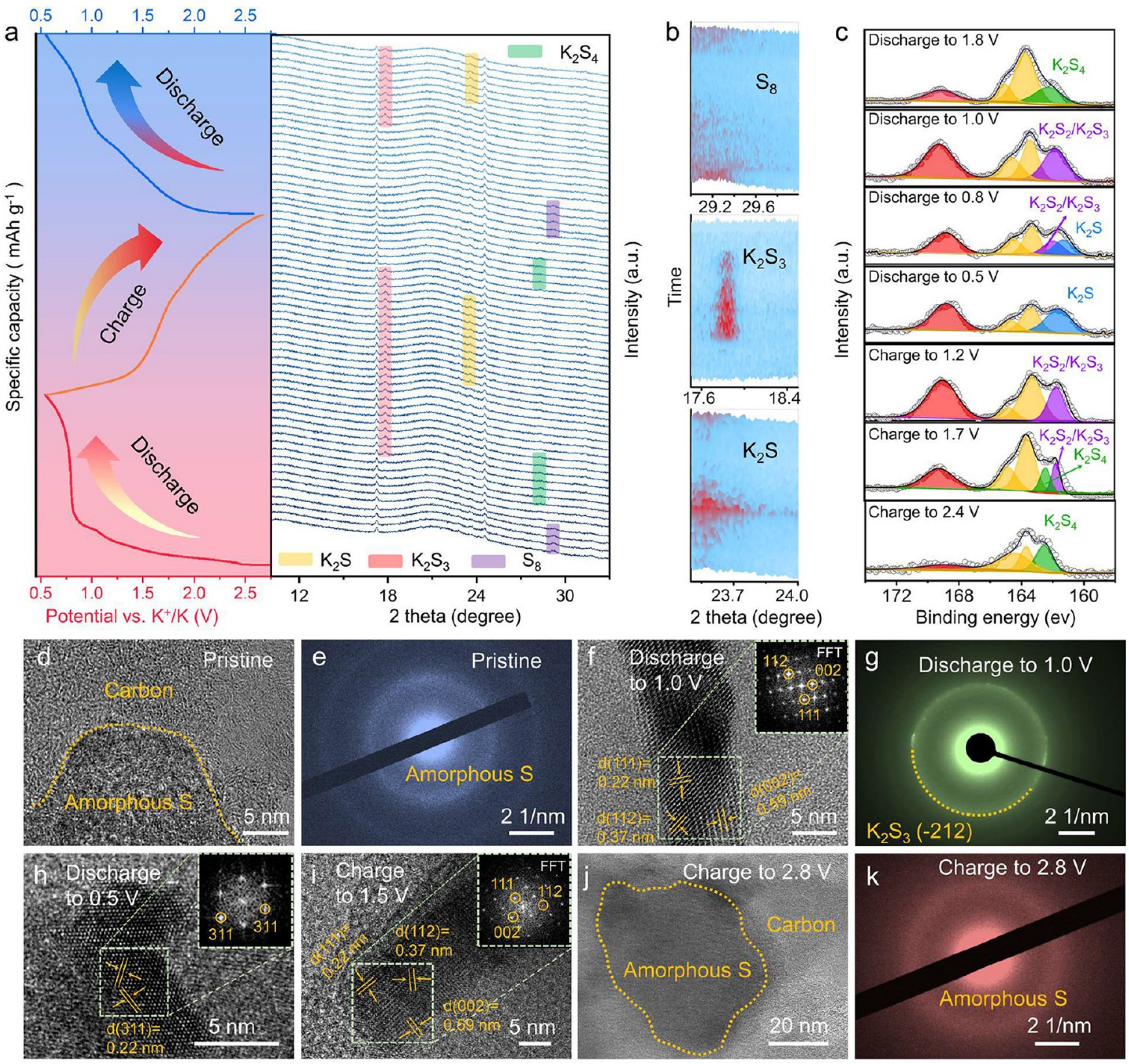

Figure 4. (a) *In situ* XRD analysis of the S/Co-GDY cathode for K−S batteries in the charging and discharging processes and (b) the corresponding contour plot of S_8, K_2S_3, and K_2S. (c) *Ex situ* high-resolution XPS spectra for the S 2p spectrum of the S/Co-GDY cathode for K−S batteries at several special charge/discharge phases. (d−k) *Ex situ* HRTEM and SAED images of the S/Co-GDY cathode at different charge/discharge states.

charge−discharge profiles of the S/Co-GDY cathode at different current densities could maintain a stable voltage plateau (Figure 3d), which is the best among the previously reported literature for K−S batteries (Figure 3e and Table S2).[9,22,24,44−47] The high redox kinetics is due to the structural advantages of the strong orbital coupling for the S/Co-GDY, resulting in a super performance at high current densities. Therefore, S/Co-GDY can deliver an even better capacity of 530 mAh g^{-1} at 1 A g^{-1} after 500 cycles with nearly 100% Coulombic efficiency and low average capacity degradation of 0.08% per cycle (Figure 3f). Even at the elevated current density of 5 A g^{-1}, S/Co-GDY still exhibits excellent cycling stability and a high discharge capacity of 158 mAh g^{-1} over 1000 cycles (Figure S18). The ultrathin GDY nanosheet still maintains a good structural integrity after the charging and discharging processes by *ex situ* TEM (Figure S19). To investigate the potential practical application of the S/Co-GDY cathode in K−S batteries, we assembled a K−S pouch cell using S/Co-GDY as cathode and potassium metal as anode, which can keep the light-emitting diode (LED, Figure 3g) on. Figure S20 displays the charge/discharge curves and cycling performance of the Co-GDY for K−S batteries in the voltage range of 0.5−2.8 V. After 100 cycles, only reversible capacities of 1.2 and 0.7 mAh g^{-1} at 0.2 and 1 A g^{-1} are achieved, indicating the capacity contribution from the Co-GDY in the S/Co-GDY composite is negligible.

The S/Co-GDY and S/GDY cathode-based RT Na−S batteries were investigated. Figures S21 and S22 exhibit CV curves at 0.1 mV s^{-1} and galvanostatic charge−discharge profiles at 0.2 A g^{-1} of S/Co-GDY and S/GDY cathodes with a voltage window of 0.8−3.0 V (vs Na$^+$/Na). The S/Co-GDY cathode reveals a higher charge capacity of 1169 mAh g^{-1} at 0.2 A g^{-1} over 100 cycles than the S/Co-GDY cathode (Figure S23a). Figures S23b,c and S24 demonstrate the excellent cycling stability and rate ability performance for Na−S batteries, outperforming the reported materials (Figure S24d and Table S3).[48−55]

To probe the reaction mechanisms and phase evolution of S/Co-GDY during the discharging and charging processes for K−S batteries, the *in situ* XRD, *ex situ* XPS, *ex situ* high-

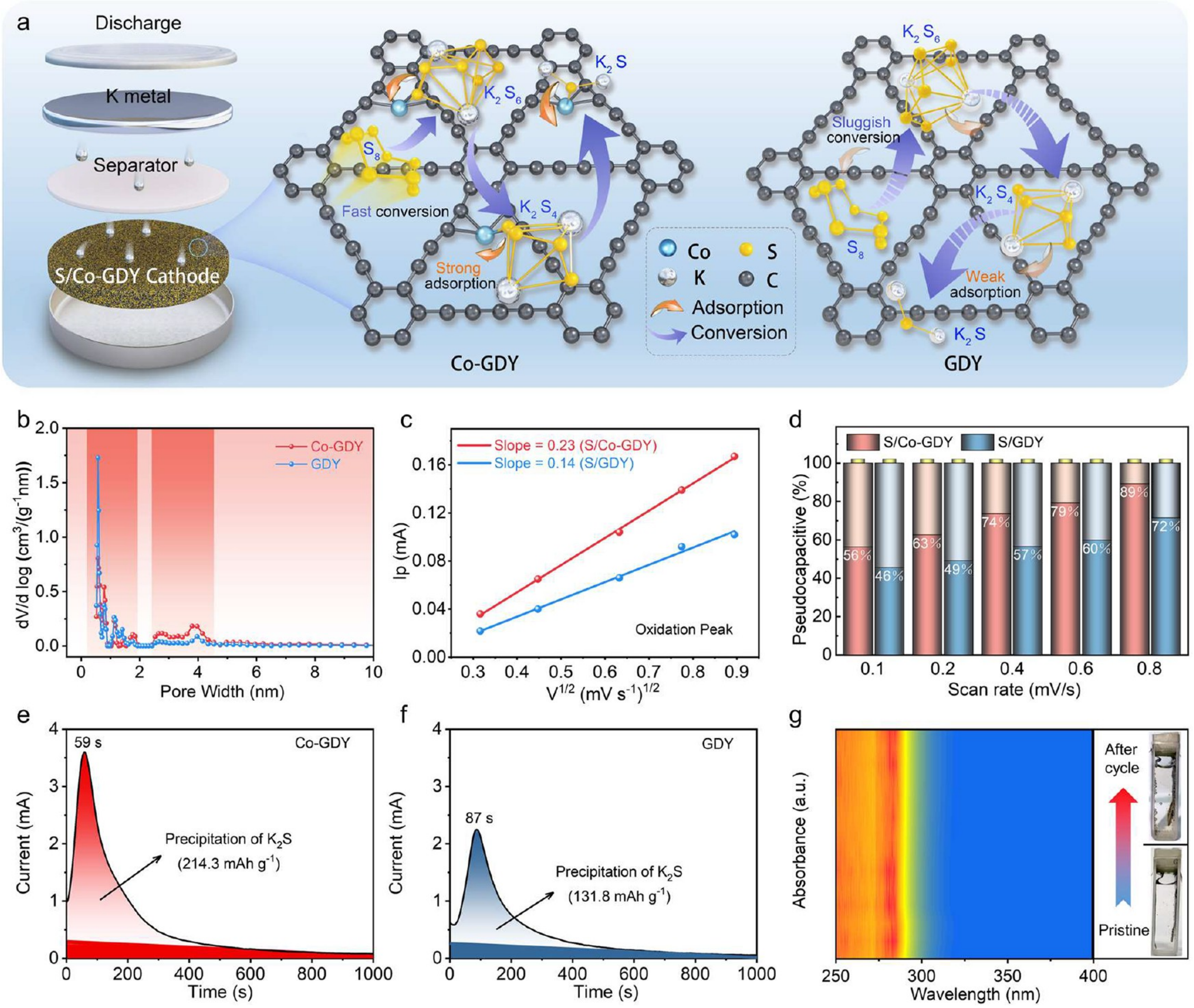

Figure 5. (a) Schematics of potassium polysulfide adsorption and conversion behaviors on different carriers of Co-GDY and GDY. (b) Pore-size distribution of the Co-GDY and GDY nanosheets. (c) Fitted lines of the oxidation peak for the S/Co-GDY and S/GDY cathodes between I_p and $v^{1/2}$. (d) The contribution ratio of capacitance/diffusion-controlled for S/Co-GDY and S/GDY cathodes under various scan rates (0.1−0.8 mV s^{-1}). (e, f) The potentiostatic discharge curves (K_2S_6-EC) of the Co-GDY and GDY samples. (g) The *in situ* UV−vis spectra of the S/Co-GDY cathode during the first discharging and charging processes. Inset: the optical images of corresponding K−S cell devices at the initial condition and after cycling.

resolution TEM (HRTEM), and *ex situ* selected area electron diffraction (SAED) were performed (Figure 4). As shown in Figure 4a,b, when the K−S battery was discharged to about 1.75 V, the characteristic peaks of S disappeared, and another characteristic peak of K_2S_4 (JCPDS No. 43-0795) appeared, attributed to the conversion from S_8 to long-chain potassium polysulfide. As the discharge voltage decreased to 1.0 V, the new diffraction peak at 17.9° attributed to K_2S_3 (JCPDF No. 30-0994) appeared. When the battery continued to discharge to 0.5 V, a new characteristic peak of K_2S (JCPDF No. 47-1702) appeared. Upon a subsequent charging process, the characteristic peaks of the K_2S_3 and K_2S appeared. These results indicate that the charging/discharging process of K−S batteries is highly reversible, involving a conversion from solid S_8 to soluble potassium polysulfide (K_2S_4) and subsequently to insoluble K_2S_3 and K_2S, demonstrating the efficient conversion ability of solid−solid reactions from K_2S_3 to K_2S. In the subsequent second discharging stages, the reduction products of K_2S_3 and K_2S were detected, indicating the excellent reversible solid−solid transformation process. To further verify the mechanism of S/Co-GDY, the *ex situ* XPS in different voltage states was investigated (Figure 4c). The diffraction peaks of the four specific discharge stages (1.8, 1.0, 0.8, and 0.5 V) correspond to K_2S_4, K_2S_3, K_2S_2, and K_2S, respectively, indicating the transformation process of $S_8 \rightarrow K_2S_4 \rightarrow K_2S_3/K_2S_2 \rightarrow K_2S$. Similarly, three charging stages (1.2, 1.7, and 2.4 V) correspond to the conversion product of K_2S_2, K_2S_3, and K_2S_4, proving a reversible conversion reaction of $K_2S \rightarrow K_2S_2/K_2S_3 \rightarrow K_2S_4 \rightarrow S_8$. The structural evolution of the S/Co-GDY during the sulfur conversion process was investigated by *ex situ* HRTEM and SAED (Figure 4d−k). At the initial stage, the amorphous structure of S was observed (Figure 4d,e). When the discharge voltage decreased to 1.0 V, the HRTEM image and fast Fourier transform (FFT) pattern established the

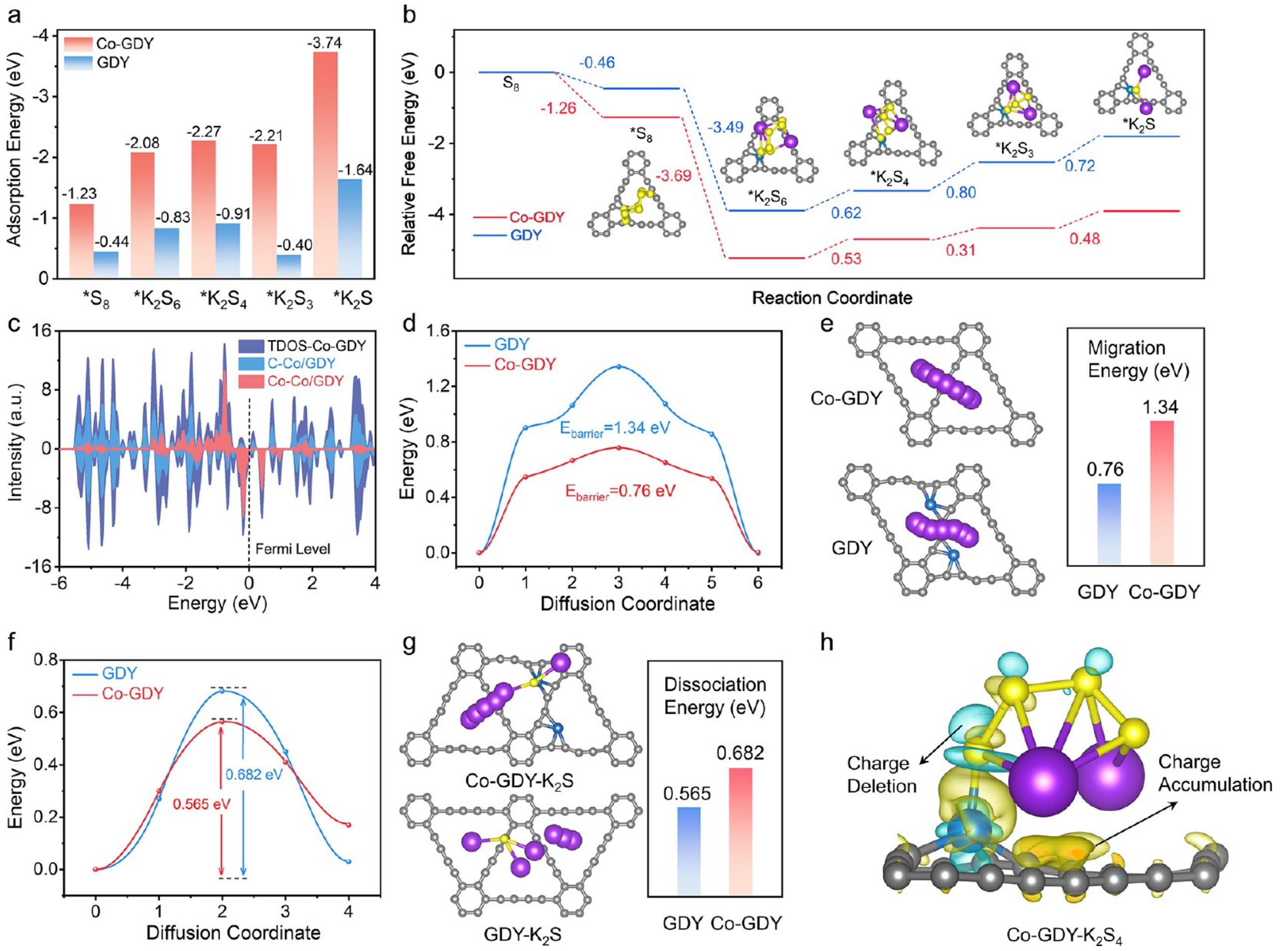

Figure 6. (a) Adsorption energy of S_8 and different potassium polysulfides adsorbed on Co-GDY and GDY. (b) Corresponding Gibbs free energy profiles with the optimized adsorption conformations in the inset. (c) The TDOS image of Co and C elements in the Co-GDY. (d, e) Energy profiles of K-ion migrations on the surfaces of Co-GDY and GDY. (f, g) Dissociation energy of K_2S on the Co-GDY and GDY substrates. (h) The charge density differences of K_2S_4 on the surfaces of Co-GDY.

formation of the K_2S_3 phase (Figure 4f,g). The lattice fringes of 0.22, 0.37, and 0.59 nm are well assigned to the (111), (002), and (112) planes of a (1, −1, 0)-oriented triclinic structure. In addition, the diffraction ring of K_2S_3 (−212) was observed in the corresponding SAED image. Upon discharge to 0.5 V, the formation of the K_2S phase was verified by the HRTEM image and corresponding FFT pattern (Figure 4h). When the battery is recharged to 1.5 V, the lattice spacing and corresponding FFT pattern were assigned to the K_2S_3 phase, demonstrating that the K_2S can be transformed into the K_2S_3 phase in the charging state of 1.5 V (Figure 4i). Subsequently, the electrode material can be converted back to amorphous S during the charging stage of 2.8 V (Figure 4j,k). The results of the *ex situ* HRTEM and SAED images were in good agreement with the results of the *in situ* XRD and *ex situ* XPS analysis. The discharge product K_2S was clearly detected, demonstrating that Co−C_4 atomic sites can effectively promote reversible solid−solid reaction kinetics by the strong d−π orbital coupling during the charging and discharging processes of the K−S battery. To verify the stability of K_2S_3 powder in the K−S battery electrolyte, the pure-phase K_2S_3 was synthesized and added to the 3 M KTFSI EC electrolyte (Figure S25), observing the clear electrolyte with the K_2S_3 powder precipitating to the bottom.[21] As shown in Figure S26, when the K−S batteries discharged to 1.0 and 0.5 V and change to 1.2 V, the Raman spectra of S/Co-GDY electrodes show three diffraction peaks corresponding to the D-band, G-band, and −C≡C−C≡C−, respectively. The diffraction peaks of −C≡C−C≡C− were detected at different charging/discharging voltages, proving the structural stability of Co-GDY during the cycling process of K−S batteries.

The strong d−π orbital coupling of the Co−C_4 atomic sites on the GDY can facilitate the charge transfer from Co to GDY, thus enhancing the adsorption and transformation of sulfur on Co atoms and improving the rate performance of the S/Co-GDY cathode for K−S batteries and RT Na−S batteries (Figure 5a). The ultrathin GDY nanosheets with a large specific surface area (817 m^2 g^{-1}) and abundant micropore (0.6−1.8 nm), and mesopore region (2.5−4.5 nm) can adsorb more sulfur and potassium polysulfide (Figures 5b, S27, and S28). The unique π-coordination structure advantage of the Co-GDY can be reflected by the faster potassium ion diffusion coefficient (Figures 5c, S29, and S30) and the higher pseudocapacitance contribution (Figures 5d, S31, and S32). Significantly, the detailed calculation processes of the *b* values, *D* values, k_1v, and $k_2v^{1/2}$ are documented in the Supporting Information. Additionally, the sodium ion diffusion capacity and the conversion efficiency of S/Co-GDY for Na−S batteries are also certified (Figures S33−S37).[56,57]

Figure 5e,f display the K_2S precipitation experiments by Faraday's law. And the S/Co-GDY cathode reveals the upper K_2S precipitation capacity of 214.3 mAh g^{-1} and the faster response time of 59 s than the S/GDY cathode (a K_2S precipitation capacity of 131.8 mAh g^{-1} and a time response of 87 s), demonstrating the super redox capability due to the strong d−π orbital coupling of the Co−C_4 atomic sites. Moreover, the *in situ* UV−vis spectra of the S/Co-GDY cathode for K−S batteries were conducted to observe the amount of potassium polysulfide in the electrolyte during the first charging and discharging processes (Figure 5g). Neither the diffraction peak in the UV−vis spectra nor the optical photograph (inset) of the K−S electrolyte after cycling shows any significant change, indicating that no significant potassium polysulfide precipitates during the charging and discharging processes, demonstrating the stable blocking effect from single-atom Co and the GDY nanosheet upon the release of potassium polysulfide.

To further investigate the electrochemical catalytic capability and the inhibition of potassium polysulfide shuttling for Co−C_4 atomic sites on GDY in the K−S batteries, DFT calculations were conducted. Figures S38 and S39 show the optimized model structure diagrams of the Co-GDY, GDY, K_2S, K_2S_3, K_2S_4, K_2S_6, and S_8, respectively. The adsorption energies of S_8 and K_2S_x (x = 6, 4, 3, 1) on the surface of the Co-GDY and GDY are shown in Figure 6a, respectively. Each K_2S_x species displays stronger adsorption energy on the Co-GDY surface than those of the GDY, suggesting the superior adsorption capacity of Co−C_4 atomic sites as the active center on GDY surfaces and the greater ability to suppress the shuttling phenomenon of K_2S_x. Then, K_2S exhibits the strongest adsorption energy of all the K_2S_x species, which favors the nucleation of K_2S. The Gibbs free energy based on the reversible conversion reaction from S_8 to K_2S was calculated and is shown in Figure 6b, and the intermediate structures of K_2S_x on the Co-GDY and GDY surfaces are provided in the inset and Figure S40. The redox ability of Co-GDY for K_2S_x species was enhanced due to the strong d−π orbital coupling of the Co−C_4 atomic sites, resulting in the reaction energy barrier for the conversion of K_2S_6 to K_2S being significantly reduced. Moreover, the electron localization function (ELF, isosurface level = 0.5) of the K_2S_6 on Co-GDY and GDY models is shown in Figure S41, indicating that the bonds between K_2S_6 and Co-GDY/GDY were all ionic bonds. The Co-GDY demonstrates a larger total density of states (TDOS) around the Fermi level than that of GDY (Figure S42), leading to the higher redox activity on the Co-GDY surface during electrochemical reactions. Further analysis of the DOS of the Co and C elements for Co-GDY reveals that Co has a larger contribution near the Fermi level, demonstrating the electron-accepting/donating capacity of Co−C_4 atomic sites via d−π orbital coupling, which benefits the more rapid electron transfer of electrons to potassium polysulfide and promotes the sulfur redox reactions (Figure 6c).

The energy barriers of K-ion migrations on the surfaces of Co-GDY and GDY were investigated to be 1.34 and 0.76 eV, respectively (Figure 6d,e), implying that the K-ion can readily migrate on the Co-GDY surface. Figure 6f,g and Table S4 compare the energy barrier of K_2S decomposition on Co-GDY (0.682 eV) and GDY (0.565 eV) surfaces to simulate the K_2S oxidation process, demonstrating the more rapid conversion efficiency of K_2S under the π-coordination structural advantage of Co−C_4 atomic sites. In addition, Figure S43 analyzes the DOS of S in K_2S_6 on Co-GDY and GDY surfaces and shows the higher DOS of S adsorption on the Co-GDY surface near the Fermi level, further proving the Co−C_4 π-coordination structure on Co-GDY can more easily reduce the K_2S_6. Figure S44 presents the crystal orbital Hamilton population (COHP) of the K−S bond in K_2S_6 adsorbed on the Co-GDY and GDY surfaces, respectively. The K−S bonds on the Co-GDY surface show the antibonding state (near −0.23 eV) below the Fermi level, and the K−S bonds on the GDY surface exhibit two stronger bonding states (near −0.54 and −1.25 eV) than that of the Co-GDY surface, indicating the Co−C_4 of Co-GDY as the catalytic active center can activate K_2S_6 and break the K−S bonds. Figures 6h, S45, and S46 compare the electron deletion and accumulation of K_2S_4/K_2S_6 around the Co-GDY and GDY surfaces, respectively, and stronger electron interactions exist between K_2S_4/K_2S_6 and Co-GDY. The strong charge transfer capability between Co-GDY and potassium polysulfide reveals that the Co−C_4 atomic sites can greatly facilitate the conversion from sulfur to potassium polysulfide. Therefore, the solid−liquid−solid redox kinetics of the Co-GDY cathode for K−S batteries can be dramatically accelerated by the strong d−π orbital coupling of Co−C_4 atomic sites, enabling more stable and efficient sulfur-based electrochemistry.

CONCLUSIONS

In summary, we have designed and synthesized a new class of Co−C_4 atomic sites on ultrathin GDY nanosheets via π-coordination as a superior sulfur host (S/Co-GDY) for advanced K−S batteries. The porous GDY nanosheets with unique sp- and sp^2-hybridized carbon atoms and a highly π-conjugated structure can precisely regulate the coordination environment of single-atom Co to enhance the catalytic ability. Synchrotron radiation XAS and DFT calculations reveal the charge transfer mechanism of the Co−C_4 active center is the charge transfer from the d-orbital of Co to the π-orbital of the sp-hybridized carbon atoms to form strong d−π orbital coupling because of high electronegativity and strong electron-withdrawing ability of $-C\equiv C-C\equiv C-$ in GDY. The charge deletion of the d-orbital can be coupled to the p-orbital of sulfur, thereby promoting the adsorption and conversion of sulfur on Co atoms. Due to the strong d−π orbital coupling of the Co−C_4 moiety, the designed Co-GDY cathode can restrict the dissolution of the potassium polysulfide and the shuttle effect, further accelerating charge transfer and redox kinetics for K−S batteries. As a result, the K−S batteries of the S/Co-GDY cathode provide a remarkable cycling performance (1064 mAh g^{-1} at 0.2 A g^{-1} after 180 cycles) and rate capability (496 mAh g^{-1} at 5 A g^{-1}).

ASSOCIATED CONTENT

Supporting Information

The Supporting Information is available free of charge at https://pubs.acs.org/doi/10.1021/jacs.3c09533.

Detailed experimental procedures, characterization methods, theoretical calculation details, other supporting results, and electrochemical measurements (PDF)

AUTHOR INFORMATION

Corresponding Authors

Yan Yu − *Hefei National Research Center for Physical Sciences at the Microscale, Department of Materials Science and*

Engineering, CAS Key Laboratory of Materials for Energy Conversion, University of Science and Technology of China, Hefei, Anhui 230026, China; orcid.org/0000-0002-3685-7773; Email: yanyumse@ustc.edu.cn

Shaojun Guo − *School of Materials Science and Engineering, Peking University, Beijing 100871, China;* orcid.org/0000-0003-4427-6837; Email: guosj@pku.edu.cn

Jin Zhang − *School of Materials Science and Engineering, Peking University, Beijing 100871, China; Center for Nanochemistry, Beijing Science and Engineering Center for Nanocarbons, Beijing National Laboratory for Molecular Sciences, College of Chemistry and Molecular Engineering, Peking University, Beijing 100871, China;* orcid.org/0000-0003-3731-8859; Email: jinzhang@pku.edu.cn

Authors

Shipeng Zhang − *School of Materials Science and Engineering, Peking University, Beijing 100871, China*

Ya Kong − *Center for Nanochemistry, Beijing Science and Engineering Center for Nanocarbons, Beijing National Laboratory for Molecular Sciences, College of Chemistry and Molecular Engineering, Peking University, Beijing 100871, China; China Academy of Aerospace Science and Innovation, Beijing 100176, China*

Yu Gu − *School of Materials Science and Engineering, Peking University, Beijing 100871, China*

Ruilin Bai − *Hefei National Research Center for Physical Sciences at the Microscale, Department of Materials Science and Engineering, CAS Key Laboratory of Materials for Energy Conversion, University of Science and Technology of China, Hefei, Anhui 230026, China*

Menggang Li − *School of Materials Science and Engineering, Peking University, Beijing 100871, China*

Shuoqing Zhao − *School of Materials Science and Engineering, Peking University, Beijing 100871, China*

Mingze Ma − *Hefei National Research Center for Physical Sciences at the Microscale, Department of Materials Science and Engineering, CAS Key Laboratory of Materials for Energy Conversion, University of Science and Technology of China, Hefei, Anhui 230026, China*

Zhen Li − *Hefei National Research Center for Physical Sciences at the Microscale, Department of Materials Science and Engineering, CAS Key Laboratory of Materials for Energy Conversion, University of Science and Technology of China, Hefei, Anhui 230026, China*

Lingyou Zeng − *School of Materials Science and Engineering, Peking University, Beijing 100871, China*

Daping Qiu − *School of Materials Science and Engineering, Peking University, Beijing 100871, China;* orcid.org/0000-0003-4245-5495

Qinghua Zhang − *Beijing National Laboratory for Condensed Matter Physics, Institute of Physics, Chinese Academy of Sciences, Beijing 100190, China*

Mingchuan Luo − *School of Materials Science and Engineering, Peking University, Beijing 100871, China*

Lin Gu − *Beijing National Laboratory for Condensed Matter Physics, Institute of Physics, Chinese Academy of Sciences, Beijing 100190, China;* orcid.org/0000-0002-7504-031X

Complete contact information is available at: https://pubs.acs.org/10.1021/jacs.3c09533

Author Contributions

S.Z. and Y.K. contributed equally to this paper

Notes

The authors declare no competing financial interest.

■ ACKNOWLEDGMENTS

This study was financially supported by National Key R&D Program of China (No. 2022YFE0128500 and 2022YFA1504100), Ministry of Science and Technology of China (2022YFA1203302, 2022YFA1203304 and 2018YFA0703502), National Science Fund for Distinguished Young Scholars (No. 52025133), National Natural Science Foundation of China (52261135633, 51925207, 52202201, U1910210, 52161145101, 52021006), the National Synchrotron Radiation Laboratory (KY2060000173), the Strategic Priority Research Program of CAS (XDB36030100), and the Beijing National Laboratory for Molecular Sciences (BNLMS-CXTD-202001), the Joint Fund of Yulin University and the Dalian National Laboratory for Clean Energy (Grant YLU-DNL Fund 2021002), the Fundamental Research Funds for the Central Universities (WK2060140026), China National Petroleum Corporation-Peking University Strategic Cooperation Project of Fundamental Research, the Beijing Natural Science Foundation (No. Z220020), New Cornerstone Science Foundation through the XPLORER PRIZE, CNPC Innovation Found (2021DQ02-1002), Hefei Municipal Natural Science Foundation (2022021), the National Postdoctoral Program for Innovative Talents (BX20220015), and the China Postdoctoral Science Foundation (2022M720002). This work was carried out with the support of the 1W1B beamline at the Beijing Synchrotron Radiation Facility.

■ REFERENCES

(1) Armand, M.; Tarascon, J. M. Building better batteries. *Nature* **2008**, *451*, 652.

(2) Grey, C. P.; Tarascon, J. M. Sustainability and in situ monitoring in battery development. *Nat. Mater.* **2017**, *16*, 45−56.

(3) Dunn, B.; Kamath, H.; Tarascon, J.-M. Electrical Energy Storage for the Grid: A Battery of Choices. *Science* **2011**, *334*, 928.

(4) Hosaka, T.; Kubota, K.; Hameed, A. S.; Komaba, S. Research Development on K-Ion Batteries. *Chem. Rev.* **2020**, *120*, 6358−6466.

(5) Fang, R.; Xu, J.; Wang, D. Covalent fixing of sulfur in metal-sulfur batteries. *Energy & Environ. Sci.* **2020**, *13*, 432−471.

(6) Ding, J.; Zhang, H.; Fan, W.; Zhong, C.; Hu, W.; Mitlin, D. Review of Emerging Potassium-Sulfur Batteries. *Adv. Mater.* **2020**, *32*, 1908007.

(7) Shao, J.; Zheng, J.; Qin, L.; Zhang, S.; Ren, Y.; Wu, Y. K_3SbS_4 as a Potassium Superionic Conductor with Low Activation Energy for K-S Batteries. *Angew. Chem., Int. Ed.* **2022**, *61*, No. e202200606.

(8) Lee, S.; Park, H.; Rizell, J.; Kim, U.; Liu, Y.; Xu, X.; Xiong, S.; Matic, A.; Zikri, A.; Kang, H.; Sun, Y.; Kim, J.; Hwang, J. High-Energy and Long-Lifespan Potassium-Sulfur Batteries Enabled by Concentrated Electrolyte. *Adv. Funct. Mater.* **2022**, *32*, 2209145.

(9) Xiong, P.; Han, X.; Zhao, X.; Bai, P.; Liu, Y.; Sun, J.; Xu, Y. Room-Temperature Potassium-Sulfur Batteries Enabled by Microporous Carbon Stabilized Small-Molecule Sulfur Cathodes. *ACS Nano* **2019**, *13*, 2536−2543.

(10) Pang, Q.; Shyamsunder, A.; Narayanan, B.; Kwok, C. Y.; Curtiss, L. A.; Nazar, L. F. Tuning the electrolyte network structure to invoke quasi-solid state sulfur conversion and suppress lithium dendrite formation in Li-S batteries. *Nat. Energy* **2018**, *3*, 783−791.

(11) Li, Z.; Samim, I.; Yang, J.; Li, J.; Kumar, R. V.; Chhowalla, M. Lithiated metallic molybdenum disulfide nanosheets for high-performance lithium-sulfur batteries. *Nat. Energy* **2023**, *8*, 84−93.

(12) Zheng, X.; Gao, X.; Vilá, R. A.; Jiang, Y.; Wang, J.; Xu, R.; Zhang, R.; Xiao, X.; Zhang, P.; Greenburg, L. C.; Yang, Y.; Xin, H. L.; Zheng, X.; Cui, Y. Hydrogen-substituted graphdiyne-assisted ultrafast sparking synthesis of metastable nanomaterials. *Nat. Nanotechnol.* **2023**, *18*, 153−159.

(13) Peng, L.; Wei, Z.; Wan, C.; Li, J.; Chen, Z.; Zhu, D.; Baumann, D.; Liu, H.; Allen, C. S.; Xu, X.; Kirkland, A. I.; Shakir, I.; Almutairi, Z.; Tolbert, S.; Dunn, Bruce; Huang, Y.; Sautet, P.; Duan, X. A fundamental look at electrocatalytic sulfur reduction reaction. *Nat. Catal.* **2020**, *3*, 762−770.

(14) Hua, W.; Li, H.; Pei, C.; Xia, J.; Sun, Y.; Zhang, C.; Lv, W.; Tao, Y.; Jiao, Y.; Zhang, B.; Qiao, S.; Wan, Y.; Yang, Q. Selective Catalysis Remedies Polysulfide Shuttling in Lithium-Sulfur Batteries. *Adv. Mater.* **2021**, *33*, 2101006.

(15) Peng, H.; Zhang, G.; Chen, X.; Zhang, Z.; Xu, W.; Huang, J.; Zhang, Q. Enhanced Electrochemical Kinetics on Conductive Polar Mediators for Lithium-Sulfur Batteries. *Angew. Chem., Int. Ed.* **2016**, *55*, 12990−12995.

(16) Wang, L.; Hua, W.; Wan, X.; Feng, Z.; Hu, Z.; Li, H.; Niu, J.; Wang, L.; Wang, A.; Liu, J.; Lang, X.; Wang, G.; Li, W.; Yang, Q.; Wang, W. Design Rules of a Sulfur Redox Electrocatalyst for Lithium-Sulfur Batteries. *Adv. Mater.* **2022**, *34*, 2110279.

(17) Zhou, T.; Lv, W.; Li, J.; Zhou, G.; Zhao, Y.; Fan, S.; Liu, B.; Li, B.; Kang, F.; Yang, Q. *Energy Environ. Sci.* **2017**, *10*, 1694−1703.

(18) Yu, X.; Manthiram, A. A reversible nonaqueous room-temperature potassium-sulfur chemistry for electrochemical energy storage. *Energy Storage Mater.* **2018**, *15*, 368−373.

(19) Vijaya Kumar Saroja, A. P.; Xu, Y. Carbon materials for Na-S and K-S batteries. *Matter* **2022**, *5*, 808−836.

(20) Hua, W.; Shang, T.; Li, H.; Sun, Y.; Guo, Y.; Xia, J.; Geng, C.; Hu, Z.; Peng, L.; Han, Z.; Zhang, C.; Lv, W. Optimizing the p charge of S in p-block metal sulfides for sulfur reduction electrocatalysis. *Nat. Catal.* **2023**, *6*, 174−184.

(21) Gu, S.; Xiao, N.; Wu, F.; Bai, Y.; Wu, C.; Wu, Y. Chemical Synthesis of K_2S_2 and K_2S_3 for Probing Electrochemical Mechanisms in K-S Batteries. *ACS Energy Lett.* **2018**, *3*, 2858−2864.

(22) Ye, C.; Shan, J.; Chao, D.; Liang, P.; Jiao, Y.; Hao, J.; Gu, Q.; Davey, K.; Wang, H.; Qiao, S. Catalytic Oxidation of K_2S via Atomic Co and Pyridinic N Synergy in Potassium-Sulfur Batteries. *J. Am. Chem. Soc.* **2021**, *143*, 16902−16907.

(23) Zhang, Y.; Kang, C.; Zhao, W.; Song, Y.; Zhu, J.; Huo, H.; Ma, Y.; Du, C.; Zuo, P.; Lou, S.; Yin, G. d-p Hybridization-Induced "Trapping-Coupling-Conversion" Enables High-Efficiency Nb Single-Atom Catalysis for Li-S Batteries. *J. Am. Chem. Soc.* **2023**, *145*, 1728−1739.

(24) Ge, X.; Di, H.; Wang, P.; Miao, X.; Zhang, P.; Wang, H.; Ma, J.; Yin, L. Metal-Organic Framework-Derived Nitrogen-Doped Cobalt Nanocluster Inlaid Porous Carbon as High-Efficiency Catalyst for Advanced Potassium-Sulfur Batteries. *ACS Nano* **2020**, *14*, 16022−16035.

(25) Ye, C.; Shan, J.; Li, H.; Kao, C.; Gu, Q.; Qiao, S. Reducing Overpotential of Solid-State Sulfide Conversion in Potassium-Sulfur Batteries. *Angew. Chem., Int. Ed.* **2023**, *62*, No. e202301681.

(26) Lai, N.-C.; Cong, G.; Lu, Y. A high-energy potassium-sulfur battery enabled by facile and effective imidazole-solvated copper catalysts. *J. Mater. Chem. A* **2019**, *7*, 20584−20589.

(27) Li, G.; Li, Y.; Liu, H.; Guo, Y.; Lia, Y.; Zhu, D. Architecture of graphdiyne nanoscale films. *Chem. Commun.* **2010**, *46*, 3256−3258.

(28) Gao, X.; Liu, H.; Wang, D.; Zhang, J. Graphdiyne: synthesis, properties, and applications. *Chem. Soc. Rev.* **2019**, *48*, 908−936.

(29) Jia, Z.; Li, Y.; Zuo, Z.; Liu, H.; Huang, C.; Li, Y. Synthesis and Properties of 2D Carbon—Graphdiyne. *Acc. Chem. Res.* **2017**, *50*, 2470−2478.

(30) Li, Y.; Xu, L.; Liu, H.; Li, Y. Graphdiyne and graphyne: from theoretical predictions to practical construction. *Chem. Soc. Rev.* **2014**, *43*, 2572−2586.

(31) Zhou, J.; Li, J.; Liu, Z.; Zhang, J. Exploring Approaches for the Synthesis of Few-Layered Graphdiyne. *Adv. Mater.* **2019**, *31*, 1803758.

(32) He, J.; Wang, N.; Cui, Z.; Du, H.; Fu, L.; Huang, C.; Yang, Z.; Shen, X.; Yi, Y.; Tu, Z.; Li, Y. Hydrogen substituted graphdiyne as carbon-rich flexible electrode for lithium and sodium ion batteries. *Nat. Commun.* **2017**, *8*, 1172.

(33) Li, J.; Yi, Y.; Zuo, X.; Hu, B.; Xiao, Z.; Lian, R.; Kong, Y.; Tong, L.; Shao, R.; Sun, J.; Zhang, J. Graphdiyne/Graphene/Graphdiyne Sandwiched Carbonaceous Anode for Potassium-Ion Batteries. *ACS Nano* **2022**, *16*, 3163−3172.

(34) Yi, Y.; Li, J.; Zhao, W.; Zeng, Z.; Lu, C.; Ren, H.; Sun, J.; Zhang, J.; Liu, Z. Temperature-Mediated Engineering of Graphdiyne Framework Enabling High-Performance Potassium Storage. *Adv. Funct. Mater.* **2020**, *30*, 2003039.

(35) Gu, Y.; Xi, B.; Tian, W.; Zhang, H.; Fu, Q.; Xiong, S. Boosting Selective Nitrogen Reduction via Geometric Coordination Engineering on Single-Tungsten-Atom Catalysts. *Adv. Mater.* **2021**, *33*, 2100429.

(36) Zou, H.; Arachchige, L.; Rong, W.; Tang, C.; Wang, R.; Tan, S.; Chen, H.; He, D.; Hu, J.; Hu, E.; Sun, C.; Duan, L. Low-Valence Metal Single Atoms on Graphdiyne Promotes Electrochemical Nitrogen Reduction via M-to-N_2 π-Backdonation. *Adv. Funct. Mater.* **2022**, *32*, 2200333.

(37) Xue, Y.; Huang, B.; Yi, Y.; Guo, Y.; Zuo, Z.; Li, Y.; Jia, Z.; Liu, H.; Li, Y. Anchoring zero valence single atoms of nickel and iron on graphdiyne for hydrogen evolution. *Nat. Commun.* **2018**, *9*, 1460.

(38) Jung, E.; Shin, H.; Lee, B.; Efremov, V.; Lee, S.; Lee, H.; Kim, J.; Antink, W.; Park, S.; Lee, K.; Cho, S.; Yoo, J.; Sung, Y.; Hyeon, T. Atomic-level tuning of Co-N-C catalyst for high-performance electrochemical H_2O_2 production. *Nat. Mater.* **2020**, *19*, 436−442.

(39) Li, J.; Han, X.; Wang, D.; Zhu, L.; Ha-Thi, M.; Pino, T.; Arbiol, J.; Wu, L.; Ghazzal, M. A Deprotection-free Method for High-yield Synthesis of Graphdiyne Powder with In Situ Formed CuO Nanoparticles. *Angew. Chem., Int. Ed.* **2022**, *61*, No. e202210242.

(40) Zhang, Y.; Huang, P.; Guo, J.; Shi, R.; Huang, W.; Shi, Z.; Wu, L.; Zhang, F.; Gao, L.; Li, C.; Zhang, X.; Xu, J.; Zhang, H. Graphdiyne-Based Flexible Photodetectors with High Responsivity and Detectivity. *Adv. Mater.* **2020**, *32*, 2001082.

(41) Liu, Y.; Sun, J.; Huang, H.; Bai, L.; Zhao, X.; Qu, B.; Xiong, L.; Bai, F.; Tang, J.; Jing, L. Improving CO_2 photoconversion with ionic liquid and Co single atoms. *Nat. Commun.* **2023**, *14*, 1457.

(42) Dostagir, N.; Rattanawan, R.; Gao, M.; Ota, J.; Hasegawa, J.; Asakura, K.; Fukouka, A.; Shrotri, A. Co Single Atoms in ZrO_2 with Inherent Oxygen Vacancies for Selective Hydrogenation of CO_2 to CO. *ACS Catal.* **2021**, *11*, 9450−9461.

(43) He, J.; Ma, S.; Zhou, P.; Zhang, C. X.; He, C.; Sun, L. Z. Magnetic Properties of Single Transition-Metal Atom Absorbed Graphdiyne and Graphyne Sheet from DFT+U Calculations. *J. Phys. Chem. C* **2012**, *116*, 26313−26321.

(44) Hu, L.; Meng, X.; Liu, L.; Liang, D.; Liang, S.; Wang, L.; Yang, L.; Ding, T.; Deng, C.; Dong, Q. A superficial sulfur interfacial control strategy for the fabrication of a sulfur/carbon composite for potassium-sulfur batteries. *Chem. Commun.* **2021**, *57*, 1490−1493.

(45) Yang, K.; Kim, S.; Yang, X.; Cho, M.; Lee, Y. Binder-Free and High-Loading Cathode Realized by Hierarchical Structure for Potassium-Sulfur Batteries. *Small Methods* **2022**, *6*, 2100899.

(46) Zhao, X.; Hong, Y.; Cheng, M.; Wang, S.; Zheng, L.; Wang, J. Xu, High performance potassium-sulfur batteries and their reaction mechanism. *J. Mater. Chem. A* **2020**, *8*, 10875−10884.

(47) Zhang, L.; Ge, L.; He, G.; Tian, Z.; Huang, J.; Wang, J.; Brett, D.; Hofkens, J.; Lai, F.; Liu, T. Tuning the Linkers in Polymer-Based Cathodes to Realize High Sulfur Content and High-Performance Potassium-Sulfur Batteries. *J. Phys. Chem. C* **2021**, *125*, 18604−18613.

(48) Wang, L.; Wang, H.; Zhang, S.; Ren, N.; Wu, Y.; Wu, L.; Zhou, X.; Yao, Y.; Wu, X.; Yu, Y. Manipulating the Electronic Structure of Nickel via Alloying with Iron: Toward High-Kinetics Sulfur Cathode for Na-S Batteries. *ACS Nano* **2021**, *15*, 15218−15228.

(49) Li, D.; Gong, B.; Cheng, X.; Ling, F.; Zhao, L.; Yao, Y.; Ma, M.; Jiang, Y.; Shao, Y.; Rui, X.; Zhang, W.; Zheng, H.; Wang, J.; Ma, C.; Zhang, Q.; Yu, Y. An Efficient Strategy toward Multichambered

Carbon Nanoboxes with Multiple Spatial Confinement for Advanced Sodium-Sulfur Batteries. *ACS Nano* **2021**, *15*, 20607−20618.

(50) Yan, Z.; Xiao, J.; Lai, W.; Wang, L.; Gebert, F.; Wang, Y.; Gu, Q.; Liu, H.; Chou, S.; Liu, H.; Dou, S. Nickel sulfide nanocrystals on nitrogen-doped porous carbon nanotubes with high-efficiency electrocatalysis for room-temperature sodium-sulfur batteries. *Nat. Commun.* **2019**, *10*, 4793.

(51) Zhang, S.; Yao, Y.; Jiao, X.; Ma, M.; Huang, H.; Zhou, X.; Wang, L.; Bai, J.; Yu, Y. Mo_2N-W_2N Heterostructures Embedded in Spherical Carbon Superstructure as Highly Efficient Polysulfide Electrocatalysts for Stable Room-Temperature Na-S Batteries. *Adv. Mater.* **2021**, *33*, 2103846.

(52) Zhang, B.; Sheng, T.; Liu, Y.; Wang, Y.; Zhang, L.; Lai, W.; Wang, L.; Yang, J.; Gu, Q.; Chou, S.; Liu, H.; Dou, S. Atomic cobalt as an efficient electrocatalyst in sulfur cathodes for superior room-temperature sodium-sulfur batteries. *Nat. Commun.* **2018**, *9*, 4082.

(53) Xiao, F.; Yang, X.; Wang, H.; Xu, J.; Liu, Y.; Yu, D.; Rogach, A. Covalent Encapsulation of Sulfur in a MOF-Derived S, N-Doped Porous Carbon Host Realized via the Vapor-Infiltration Method Results in Enhanced Sodium-Sulfur Battery Performance. *Advanced Energy Mater.* **2020**, *10*, 2000931.

(54) Li, Z.; Wang, C.; Ling, F.; Wang, L.; Bai, R.; Shao, Y.; Chen, Q.; Yuan, H.; Yu, Y.; Tan, Y. Room-Temperature Sodium-Sulfur Batteries: Rules for Catalyst Selection and Electrode Design. *Adv. Mater.* **2022**, *34*, 2204214.

(55) Zhang, E.; Hu, X.; Meng, L.; Qiu, M.; Chen, J.; Liu, Y.; Liu, G.; Zhuang, Z.; Zheng, X.; Zheng, L.; Wang, Y.; Tang, W.; Lu, Z.; Zhang, J.; Wen, Z.; Wang, D.; Li, Y. Single-Atom Yttrium Engineering Janus Electrode for Rechargeable Na-S Batteries. *J. Am. Chem. Soc.* **2022**, *144*, 18995−19007.

(56) Zhang, S.; Ling, F.; Wang, L.; Xu, R.; Ma, M.; Cheng, X.; Bai, R.; Shao, Y.; Huang, H.; Li, D.; Jiang, Y.; Rui, X.; Bai, J.; Yao, Y.; Yu, Y. An Open-Ended Ni_3S_2-Co_9S_8 Heterostructures Nanocage Anode with Enhanced Reaction Kinetics for Superior Potassium-Ion Batteries. *Adv. Mater.* **2022**, *34*, 2201420.

(57) Wei, X.; Lin, C.; Wu, C.; Qaiser, N.; Cai, Y.; Lu, A.; Qi, K.; Fu, J.; Chiang, Y.; Yang, Z.; Ding, L.; Ali, O.; Xu, W.; Zhang, W.; Hassine, M.; Kong, J.; Chen, H.; Tung, V. Three-dimensional hierarchically porous MoS_2 foam as high-rate and stable lithium-ion battery anode. *Nat. Commun.* **2022**, *13*, 6006.